Electrochimica Acta 54 (2008) 844–855

Contents lists available at ScienceDirect

Electrochimica Acta

journal homepage: www.elsevier.com/locate/electacta

# The influence of MgSi particle reactivity and dissolution processes on corrosion in Al–Mg–Si alloys

Fabian Eckermann[a,b], Thomas Suter[a], Peter J. Uggowitzer[b], Andreas Afseth[c], Patrik Schmutz[a,*]

[a] Laboratory for Corrosion and Materials Integrity, Swiss Federal Laboratories for Materials Testing and Research (EMPA), 8600 Dubendorf, Switzerland
[b] Laboratory of Metal Physics and Technology, Department of Materials, ETH Zurich, 8093 Zurich, Switzerland
[c] Alcan Inc., Voreppe 38341, France

ARTICLE INFO

*Article history:*
Received 6 March 2008
Received in revised form 29 May 2008
Accepted 30 May 2008
Available online 12 June 2008

*Keywords:*
Al–Mg–Si
$Mg_2Si$
De-alloying
Pitting corrosion
Cathodic activity

ABSTRACT

In Al–Mg–Si alloys, MgSi and Si precipitates are reported to activate corrosion processes. However, their impact is not completely clear because only indirect studies on the influence of Mg and Si on corrosion processes within Al–Mg–Si alloys are available. For this reason, a detailed electrochemical and compositional characterization of MgSi precipitates in Al–Mg–Si during corrosion processes were performed in this study. It was found that in 1 M NaCl solution, MgSi particles are selectively de-alloyed by Mg, the process starting within the first few seconds and ceasing after about 20 min. The open circuit potential of the whole surface is controlled by the active Mg dissolution within these 20 min. After de-alloying, the MgSi remnant (Si-rich) is cathodic-active. The cathodic current density is raised by a factor of 3 due to the presence of 0.6% surface fraction MgSi remnants. With regard to the anodic activity, it is seen that MgSi remnants (hole with Si enrichment) do not change the pitting potential in electrochemical micro- and macro-cell experiments. Fe-containing intermetallics can be inactive for the first minutes of immersion and then become active within about 40 min of exposure even though the mixed carbon, Al-oxide layer has not completely dissolved.



## 1. Introduction

Al–Mg–Si alloys are widely used in outer panel applications. Their characteristic properties of high specific stiffness, good formability, recycling potential and good corrosion resistance, together with good weldability, make them superior candidates for the transport sector, especially the automotive industry [1,2]. Despite the decent corrosion resistance usually obtained in Al alloys which are passive in the pH domain ranging from 3 to 8, a number of problems related to localized corrosion attack are still observed [3–5]. In addition, as a result of the low solubility limit of alloying elements intermetallics form, and these inhomogeneities play an important role in the local distribution and rate of cathodic and anodic reactions. For Al–Mg–Si alloys, intermetallics and grain boundaries are seen as the main anodic corrosion initiation sites, and most intermetallics enhance the corrosion rate due to their cathodic activity [5–11]. The main intermetallics present in Al–Mg–Si alloys are Fe-containing intermetallics (noble compared to matrix) and MgSi precipitates (ambivalent electrochemical behavior).

The influence of cathodic activity on corrosion processes can be revealed by removing all Fe-containing intermetallics from a surface by chemical dissolution. As a result, the observed filiform attack, which is strongly related to local reactivity, slows significantly down as long as no new intermetallics from the bulk are exposed to the solution. This decrease in the lateral corrosion propagation rate under an organic coating correlates with significantly reduced cathodic activity [12]. Another way of quickly detecting cathodically active phases with high lateral resolution is to use a "Ce precipitation process", which involves using cerium as a corrosion inhibitor. Concerning the inhibition mechanism offered by cerium, it is reported that an insulating cerium oxide/hydroxide layer precipitates from the solution at sites where the pH rises and thus hinders further electrochemical reactions [13–16]. This precipitation mechanism is the result of the low solubility of Ce in water at high pH and the stability of different Ce oxidation states according to potential and pH [17]. As a result of this precipitation, cathodes are deactivated as soon as the reduction reaction is sufficient enough to allow the pH to rise locally and Ce oxide decoration to occur. Care must be taken when using this method, because enhancement of the cathodic activity due to Ce may also take place when electrochemical reduction of $Ce^{4+}$ is involved in the

* Corresponding author at: EMPA Duebendorf, Laboratory for Corrosion and Materials Integrity (Abt. 136), Ueberlandstrasse 129, 8600 Duebendorf, Switzerland. Tel.: +41 44 823 4845; fax: +41 44 823 4015.
*E-mail address:* patrik.schmutz@empa.ch (P. Schmutz).

0013-4686/$ – see front matter © 2008 Published by Elsevier Ltd.
doi:10.1016/j.electacta.2008.05.078

process [18]. Nevertheless, this method for the detection of cathodic sites provides the unique possibility of fast mapping and reactivity assessment of single intermetallics in a realistic environment. Furthermore, the interfacial composition underneath the Ce precipitates of the cathodically active sites can be analyzed subsequently by surface analytical techniques.

The anodic activity of Fe-containing intermetallics is reported to be low in Al–Mg–Si alloys because they are often cathodically polarized and protected when they are exposed to conducting electrolytes. The sometimes observed de-alloying of these intermetallics [7,19,20] could be the result of chemical dissolution at high pH. Besides the influence of Fe-containing intermetallics coming directly from the melt, the influence of MgSi present as a hardening phase in different amounts and size depending on the heat treatment [21,22] has to be considered in the Al–Mg–Si alloy corrosion process. Detailed investigations of the corrosion behavior of MgSi particles have only been published recently [23–26]. In general it is reported that excess Si (leading to more MgSi precipitation), added in Al–Mg–Si alloys mainly to obtain higher mechanical strength, leads to higher intergranular corrosion susceptibility. However, high Mg content reduces corrosion propagation susceptibility but is simultaneously detrimental to formability, extrudability and strength [27,28]. The MgSi particles show, for different aluminium alloys, active anodic dissolution of Mg within seconds after immersion in aggressive chloride-containing solutions [23–25]. The initial open circuit potential measured on MgSi is about −1.5 V vs. SCE in NaCl solutions, while a potential up to −0.7 V is also reported for the same compound after longer immersion times [26]. On the impact of the MgSi morphology on corrosion, Mol et al. found that the presence of coarse MgSi decreases susceptibility to filiform attack compared to alloys with only β′ (semicoherent precursor of MgSi) precipitates [29]. Regarding the impact of MgSi on in-depth corrosion propagation, contradictory results are found in literature. Yasakau et al. [25] do not observe deep localized corrosion associated with MgSi particles, while Guillaumin and Mankowski [7] reported deep growing attack for MgSi particles. As to the anodic dissolution behavior of these particles, Wloka and Virtanen [30] and Eckermann et al. [31] also did not report MgSi as a preferential initiation site for deep penetrating corrosion attack. One of the major issues here involves a clear definition of localized attack and the separation between the mechanism of MgSi intermetallics dissolution and in-depth propagation of the resulting pits.

Besides characterization of the anodic MgSi dissolution mechanism at the outset of aggressive solution exposure, not many results on the activity of the Si remnant have been published so far. Si is reported to have an open circuit potential of −0.17 V [26], which is more noble than the open circuit potential of aluminium. Mizumo et al. [24] stated that no electrochemical activity on Si precipitates takes place. They claimed that SiO forms above the Si inclusions and, depending on the nature of the oxide, can prevent cathodic reaction. As opposed to results on cathodic activity of the Si-containing intermetallics, Si precipitation and the resulting depleted zones at grain boundaries are reported to enhance intergranular corrosion susceptibility [32] even though overall Si amount in a binary Al–Si alloy has little effect on filiform corrosion, which is related to the cathodic activity of the Al alloy surface [6].

In this work, the influence of MgSi particles on the corrosion behavior of Al–Mg–Si alloys is studied in detail to assess the importance of this phase on the corrosion process. The reactivity of Fe-containing intermetallics is also mapped and compared to the activity of MgSi particles. To clarify the role of MgSi particles in corrosion initiation or propagation, the activity of the MgSi particle was monitored during its de-alloying process. In particular, the influence on corrosion processes of the de-alloyed MgSi remnant (which is sometimes incorrectly reported as stable localized corrosion) is considered with respect to cathodic activity and related to its effect as a pit initiation site.

**Table 1**
The composition of AA6111 measured by optical emission spectroscopy

| wt% | AA6111 |
|---|---|
| Mg | 0.61 |
| Si | 0.80 |
| Fe | 0.26 |
| Mn | 0.21 |
| Cu | 0.70 |
| Cr | 0.02 |

Al balanced to 100%.

## 2. Experimental

All specimens were prepared from a commercial alloy AA6111 of the composition listed in Table 1, where Al is balanced to 100%.

The AA6111 sheet material was solution heat-treated for 15 min at 540 °C and water-quenched. Afterwards it was held at 350 °C for 15 h and 111 h, respectively, to create a condition, where a high amount of $Mg_2Si$ particles can be obtained. Besides the MgSi precipitates, the alloy AA6111 contains Al–Fe–Mn–Si intermetallics [21,22] which are mainly cubic α ($Al_{15}(Fe, Mn)_3Si_2$) and monoclinic β ($Al_5FeSi$) phase.

The distribution of Fe-containing intermetallics and the MgSi particles is shown in Fig. 1 for two different heat treatments. In Fig. 1a, a tomogram of a naturally aged specimen (T4 condition) is shown to illustrate the change in the microstructure resulting from the heat treatment applied in this work (350 °C 15 h, Fig. 1b).

The white areas in the grey Al matrix are Fe-containing intermetallics. The black areas represent low X-ray-absorbing MgSi particles. With the data obtained from X-ray microtomography, a volume fraction and surface area fraction of 0.6 ± 0.08% MgSi particles was measured for the specimen heat-treated at 350 °C for 15 h (Fig. 1b). In contrast to the high amount of MgSi particles for the high-temperature heat treatment (Fig. 1b) only a few MgSi particles are visible in T4 condition (Fig. 1a).

The advantage of using X-ray microtomography for microstrucutral analysis is that all artifacts related to sample preparation can be avoided. The information is obtained in the bulk of the material and the reactivity of the MgSi in contact with polishing solution is not an issue. In addition, three-dimensional information on the microstructure and particle distribution can be gathered.

Specimens were cut out of the sheets with a band saw and mechanically ground with SiC paper in successive steps up to 4000 grid. The specimens were polished further with 3 μm, 1 μm and with a 0.25-μm diamond paste finish. All steps in grinding and polishing were performed in ethanol to minimize dissolution occurring as a result of water exposure.

The cerium-containing solution exposure experiments for investigation of local cathodic activity were performed in 1 M NaCl solution with the addition of 10 mM $CeCl_3$.

Fig. 2 shows a solubility diagram of Ce in different oxidation states as a function of pH.

For the experiments presented in this paper, the Ce concentration was adjusted so that first precipitation occurred within the pH range where aluminum oxide is stable. The use of this pH threshold allowed detection of activity before the occurrence of trenching and chemical dissolution of Al around intermetallics. A measured Ce signal on a surface corresponds to locations where high pH values (>8) are present. In general, a high pH value is generated where cathodic activity is occurring, and therefore the Ce signal can be correlated with local cathodic activity. There are some exceptions,

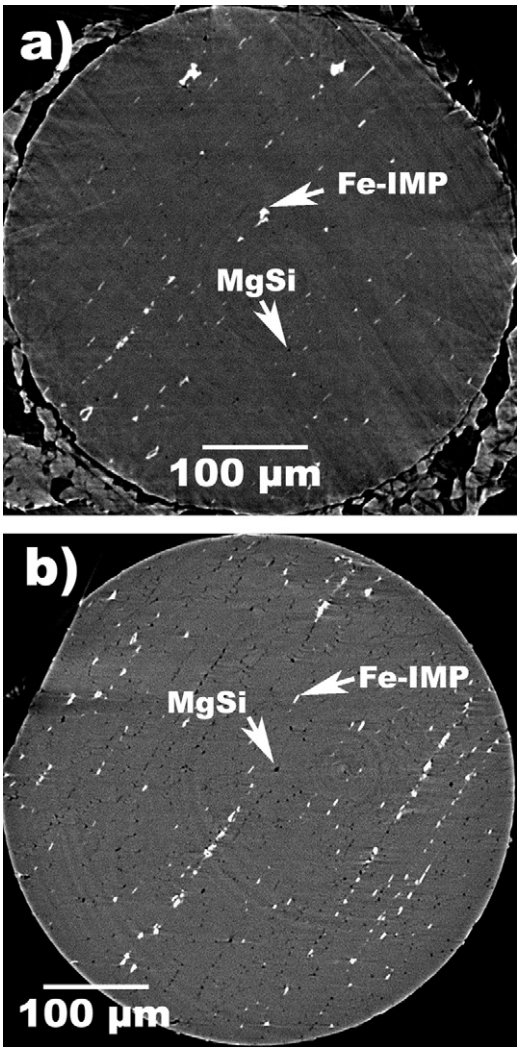


**Fig. 1.** Alloy AA6111 microstructure obtained from X-ray microtomography measurements. The grey region represents the aluminium matrix. (a) Sample in T4 condition (held at room temperature for several weeks); (b) sample heat-treated at 350 °C for 15 h, with detectable MgSi.

especially related to Mg dissolution, and these will be discussed during the presentation of the experimental results.

All specimens were exposed for 12 min to 1 M NaCl solution with the addition of 10 mM $CeCl_3$ solution. In this paper, specimens left in contact with controlled laboratory air (43% RH, 23 °C) for 1 h after polishing and before immersion in the Ce solution are called "aged". Specimens immersed in 1 M NaCl solution for 30 min prior to cerium salt addition are referred to as "precorroded".

The microstructure and Ce precipitation were investigated using an electron probe microanalysis system (EPMA) operating with a 20 kV and 20 nA electron beam and equipped with 4 wavelength dispersive X-ray detectors (JEOL JXA-8800RL). Secondary electron images, Si, Fe, Mg, and Ce maps were measured averaging over an acquisition time of 500 ms/pixel.

Auger electron spectroscopy (AES) surface characterization was performed using a PerkinElmer PHI Model 4300 Scanning Auger Microprobe equipped with a CMA analyzer (energy resolution $\Delta E/E$ of 0.6%). For all Auger measurements, an electron beam current of 100 nA at a voltage of 5 kV and an incidence angle of $48 \pm 6°$ with respect to the surface was used. All elements were detected and analyzed using their main KLL peak, except for Ce, where the main MNN peak was used. The atomic percentage was calculated using the peak-to-peak amplitude of the differentiated signal corrected with the relative sensitivity factors obtained from the PerkinElmer PHI Handbook [33]. For sputter depth profile measurements, argon ions (energy = 4.5 kV, current = 85 nA) were used in an alternating sputtering/acquisition mode. A sputter time of 9 s per cycle was used, which corresponds to the removal of a surface layer of 4.5 nm $Ta_2O_5$ equivalent per cycle. After each sputter cycle, acquisition of the specific Auger spectra of the different elements was performed.

For the electrochemical experiments, a three electrodes cell was used with a standard calomel (SCE) reference electrode inserted into a Haber–Luggin capillary and a platinum counter electrode. The sample was exposed to the solution through an opening in the side of a polymethylmethacrylate (PMMA) cell, yielding a working electrode surface area of 1 $cm^2$. Sealing to prevent loss of solution was achieved using an O-ring of natural butadiene rubber. The macroscopic potentiodynamic polarization experiments were carried out in 1 M NaCl. The sample surface was immersed for 30 min at open circuit condition and the potential was subsequently scanned with a sweep rate of 1 mV/s.

The electrochemical micro-cell experiments were performed in 1 M NaCl with 30 min exposure to solution at open circuit condition followed by the same 1 mV/s polarization rate as used in the macroscopic experiments. A pulled glass capillary with a diameter of 80 µm filled with electrolyte was placed on selected areas of the surface to perform the electrochemical characterization. A silicone coating on the tip of the capillary prevented the electrolyte from flowing out. A detailed description of the microscopic experimental setup can be found in a paper by Suter and Boehni [34].

## 3. Results and discussion

### 3.1. Overview of local reactivity of a polished surface and influence of air aging

In the first section of this paper, an overview of the local reactivity of the alloy AA6111 surface as a function of different surface conditions and solution exposure is presented.

In Fig. 3, SEM images of a freshly polished surface of aluminium alloy AA6111 (heat-treated for 15 h at 350 °C) and subsequently exposed to 1 M NaCl for various times is shown. The sequence of

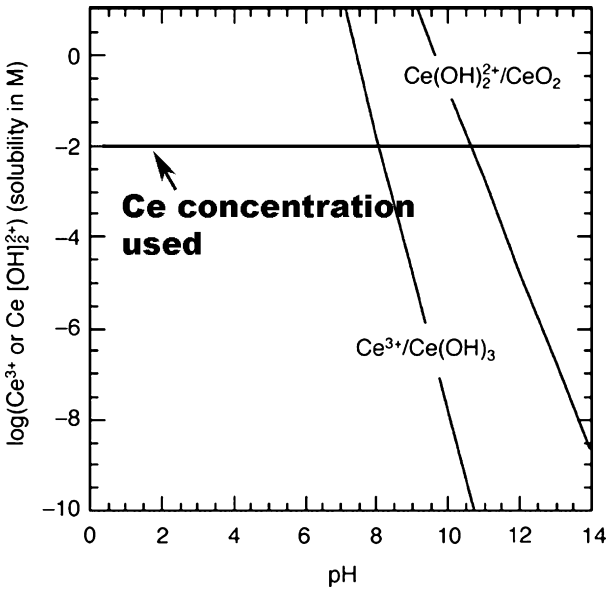


**Fig. 2.** Solubility of different Ce species in water as a function of pH. The Ce concentration used for the experiments is indicated by a line [14,17].

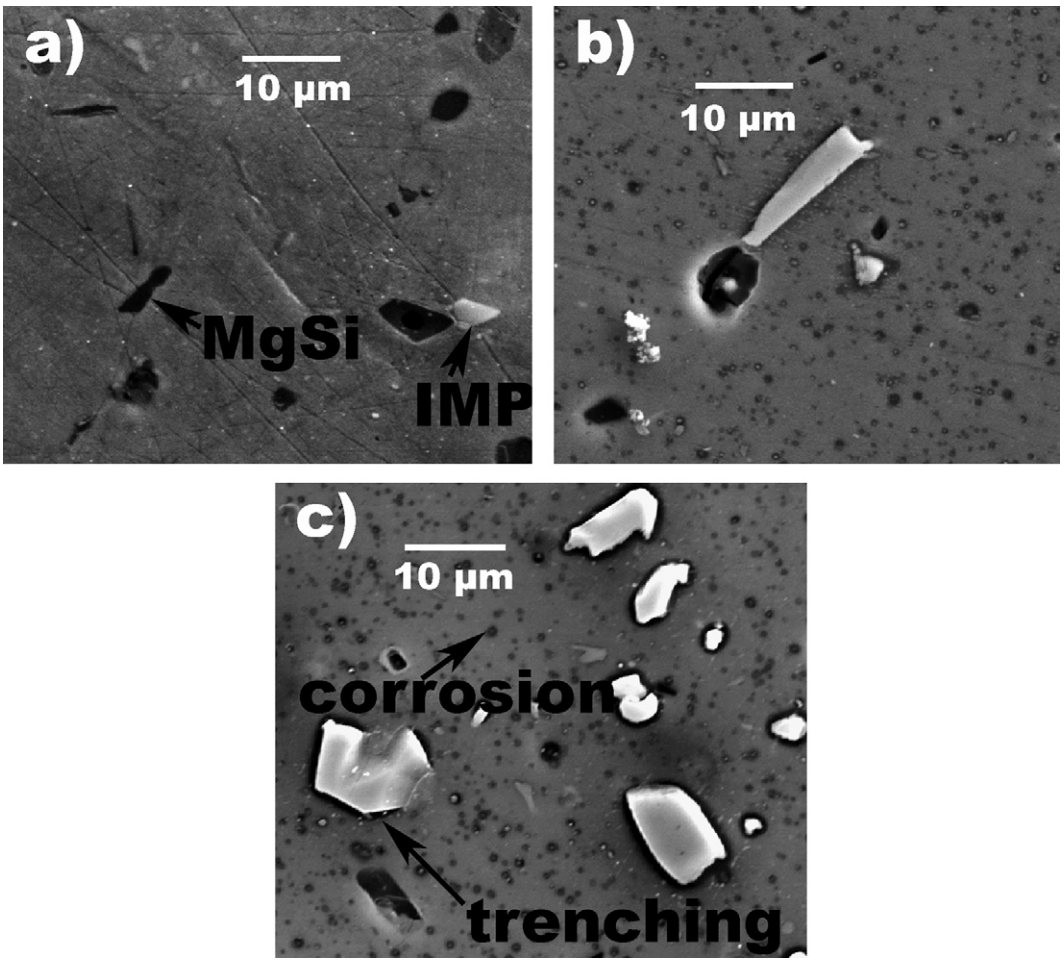


**Fig. 3.** SEM images of a freshly polished surface of AA6111 alloy (heat-treated at 350 °C for 15 h) after various periods of exposure to 1 M NaCl: (a) no exposure; (b) 10 min; (c) 30 min.

the different exposure times show the evolution in ponderosity and morphology of corrosion at MgSi- and Fe-containing intermetallics, and gives an overview of the localized corrosion processes occurring. The heat treatment conditions were chosen to obtain a large number of micrometer range MgSi precipitates. On the SEM image in Fig. 3a, taken before the surface was exposed to solution, the black areas represent MgSi particles while the bright areas are Fe-containing intermetallics.

After 10 min immersion, all MgSi particles were attacked (Fig. 3b). It can be seen that small precipitates (submicrometer range) are also corroded. These small precipitates are not detectable in the uncorroded state in a SEM image due to their submicrometer size.

After 30 min of NaCl solution exposure, significant trenching around the Fe-containing intermetallics and extensive corrosion of all MgSi particles is observed (Fig. 3c). These observations already point to the fact that MgSi precipitates are quickly anodically active regardless of size, in contrast to Fe-containing intermetallics, which may be cathodically active only after several minutes.

Anodic dissolving sites are simple to detect, but in order to map cathodically active sites and characterize the lateral distribution of active surface areas, a Ce detection method was applied as described in the experimental section. In this procedure, high pH areas on the surface are decorated with Ce, revealing cathodically active sites. The Ce concentration was adjusted such that the first precipitation occurred within the pH range of stable aluminium oxide (pH around 8). This procedure allowed detection of local surface activity before trenching and chemical dissolution of Al occurred. It was thus possible to characterize the local cathodic reactivity responsible for the initial state of corrosion.

Fig. 4 presents EPMA mappings of a surface exposed for 12 min to a 1-M NaCl solution containing 10 mM $CeCl_3$. The surface in "aged" condition, i.e., hold for 1 h in controlled laboratory air prior to immersion, which caused the modification of the oxide layer and a formation of a thin contamination layer from lab air on the surface. This aging condition was considered in order to investigate the influence of the oxide layer on the local activity of the surface.

In Fig. 4a, Fe-containing intermetallics (bright areas) and corroded MgSi (dark areas) can be seen on the secondary electron image. Deposition of Ce (Fig. 4b) does not coincide with the location of Fe-containing intermetallics for this aging condition (Fig. 4e), and it can therefore be assumed that Fe-containing intermetallics are not cathodically active within the first 12 min of solution exposure in an air-aged surface.

The Si signal mapping (Fig. 4d) also cannot be correlated with the Ce signal if the Si signal coincides with a Fe signal indicating the presence of Fe-containing intermetallics. It is only when a Si signal coincides with an Mg signal that the Ce peak is visible, and therefore when corrosion activity of MgSi particles can be concluded. As a result of this observation it may be stated with certainty that the initial dissolution rate of MgSi particles is not directly related to the cathodic activity of the Fe-containing intermetallics. MgSi particles have started to corrode even if the cathodic activity of the Fe-containing particles is still low. This mechanism was predictable

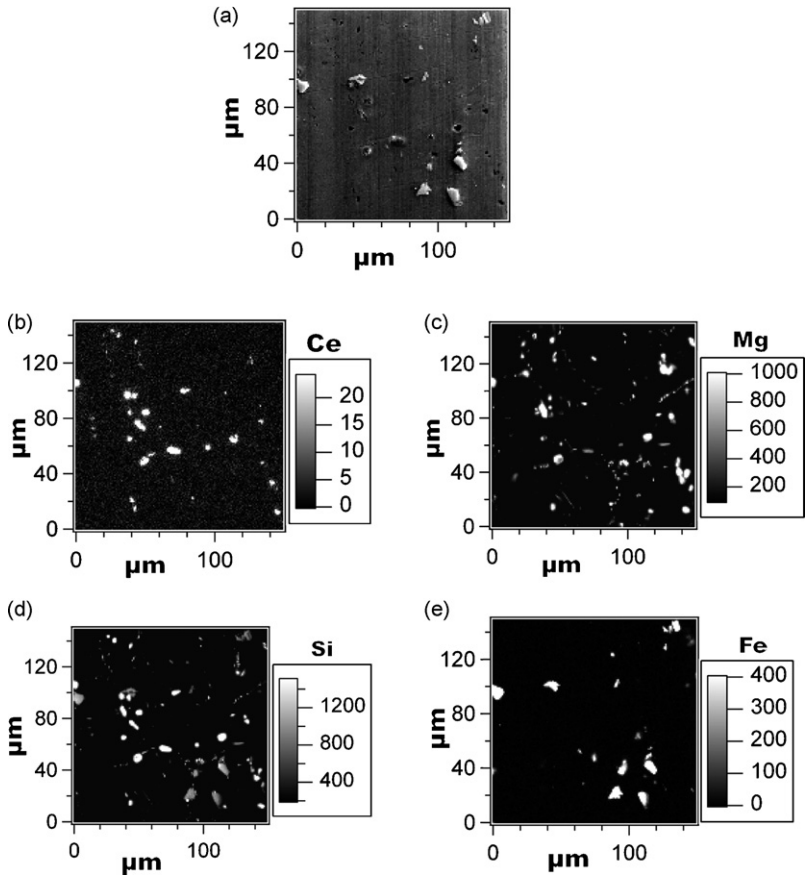


**Fig. 4.** EPMA mapping of an "aged" (1 h at laboratory air) surface immersed in 10 mM $CeCl_3$ + 1 M NaCl for 12 min. (a) SEM image; (b–e) Ce, Mg, Si, Fe element distribution.

because of the very active nature of the MgSi particles, but has never before been shown so clearly.

The presence of a Ce peak at MgSi locations also provides important new information concerning the pH evolution and local alkalinization occurring on the MgSi particles. Since Ce only precipitates at pH values above 8, the pH evolution at MgSi particles contrasts totally with the acidic environment needed for stable localized attack propagation. High pH will also provoke Al dissolution, but the hydrolysis and hydronium reduction provoked by Al ions will decrease the local high pH and reduce the Al dissolution rate within the pit such that no stable pit growth can develop and repassivation is likely. The exact mechanism inducing this high pH on actively corroding MgSi particles is not yet clear, but two hypotheses can be formulated. The first is that a high pH is the result of the active dissolution of Mg and the important hydrogen reduction rate occurring at the low potential present on MgSi surfaces [35]. The second, if we refer only to the Ce deposition experiments, may be that the cathodic activity of Si remnants after/during Mg dissolution is significant enough to allow a pH increase.

For this surface ageing condition, as already mentioned, it is interesting to note that cathodic Fe-containing intermetallics are not significantly active at the outset of solution exposure. This implies that the dissolution of the MgSi particles which are found in this study to be active within seconds can play a dominant role in the initial phase of the corrosion process. This phenomenon is especially critical as the particles are mainly aligned at grain boundaries (Figs. 4c and 5c, d) and could initiate intergranular attack. The direct observation of heavily reduced activation of Fe-containing intermetallics for short immersion times (first 12 min) has not, to the author's knowledge, been reported in literature.

In order to investigate in more detail the different reactivity of Fe-containing intermetallics and MgSi particles, the specimens were precorroded after the 1 h air aging of the surface. Fig. 5 presents element maps of a specimen surface immersed for 12 min in a Ce-containing 1 M NaCl solution after precorrosion. Due to longer immersion (30 min precorrosion in 1 M NaCl) of the AA6111 surface before adding Ce to the solution (additional 12 min in NaCl + Ce solution), the Fe-containing intermetallics (bright features in Fig. 5a) are decorated with Ce and in this way cathodic activity is detected. This active behavior contrasts with the passive behavior of Fe-containing intermetallics, which are not precorroded, as shown in Fig. 4. The observed Ce on the surface of cathodically active particles may be the result of either a transition in cathodic activity between 12 min and 42(30 + 12) min of immersion, or an integration effect of a low cathodic reaction rate (steady state is reached after long periods). The MgSi particles (dark areas in Fig. 5a) are again attacked and decorated with Ce. The precorrosion experiment allowed Mg to dissolve quickly at the beginning, leaving a Si-rich remnant before Ce deposition. The fact that Ce is deposited on these Si remnants opens the question of the cathodic reactivity of the silicon.

One drawback of the EPMA method should be mentioned here. Due to the analyzed depth in the micrometer range, elements and therefore particles present below the surface can also be detected. For example, in Fig. 5c and d, MgSi particles are detected without the presence of a corresponding Ce signal; they are also not observed in the secondary electrons image (Fig. 5a). These particles are therefore assumed to be located below the surface and not exposed to solution, and hence also show no corrosion. The Ce detection experiment was initially designed to characterize Ce

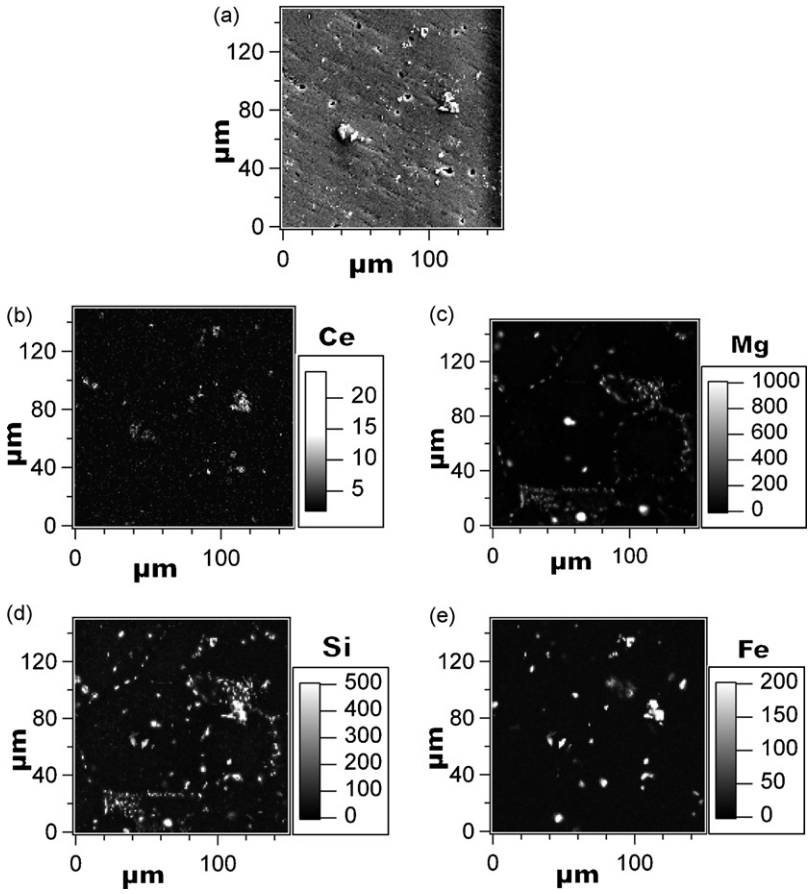


**Fig. 5.** Electron microprobe mapping of a precorroded (1 h at air, 30 min in 1 M NaCl) surface immersed in 10 mM $CeCl_3$ + 1 M NaCl for 12 min. (a) SEM image; (b–e) Ce, Mg, Si, Fe element distribution.

as an corrosion inhibitor [14], but the experimental results shown here revealed that there is much more information to be obtained this way on cathode distribution and even on anodically dissolving particles.

### *3.1.1. Surface composition and reactivity of Fe-containing intermetallics*

To explain the change in the activity of Fe-containing intermetallics, the outermost surface enabling enhanced local activity (the distribution of these sites is easily mapped with EPMA) needs to be characterized. For the investigation of small surface areas with high surface sensitivity, AES analysis has to be performed. Fig. 6 shows an AES depth profile of a Fe-containing intermetallic after precorrosion in 1 M NaCl for 30 min followed by addition of 10 mM $CeCl_3$ exposed for additional 12 min.

It can be seen that the Ce layer is about 30-nm thick and is correlated with the oxygen peak. Furthermore after about 40 nm, the Fe peak shows up. This marks the bulk intermetallic particle. An increased amount of carbon is present at the interface between the Ce layer and the alloy. This indicates that the Al-oxide and contaminations on the surface are not completely removed before Ce deposition occurs.

The observed increase in activity of the Fe-containing intermetallics as a function of solution exposure time demonstrates that the naturally formed oxide layer is a kinetic barrier. However, as shown in Fig. 6 where an aluminium oxide signal is detected together with a Ce signal in the Ce deposit, for cathodically active Fe-containing intermetallics, the AES depth profile indicates that it is not necessary to remove the whole surface oxide layer to obtain significant cathodic activity. A carbon layer underneath the Ce signal also indicates that a pH rise (=cathodic activity) took place before complete dissolution of the air-formed surface layer. Not explicitly shown in Fig. 6 is the separation between aluminium oxide present in the Ce layer and metallic Al peaks present in the bulk region. Fig. 7 shows two exemplary spectra from the surface region (18 nm below the surface) and of the bulk metallic region

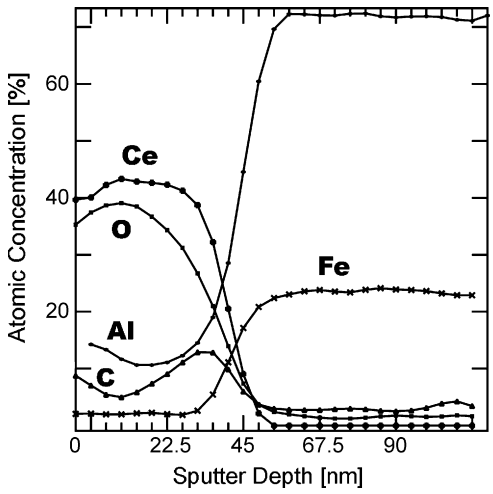


**Fig. 6.** Auger electron spectroscopy (AES) depth profile acquired on a Fe-containing intermetallic after precorrosion in 1 M NaCl for 30 min followed by addition of 10 mM $CeCl_3$ exposed and additional exposure of 12 min.

(81 nm below the surface). The oxidized Al peak position is clearly shifted by $\Delta E = 3$ eV compared to the metal peak position in the bulk of the intermetallics (Fig. 7). From this result, it can be assumed that Al oxide is present in the whole mixed layer.

Because the MgSi particles are, in opposite to the Fe-containing intermetallics, in all conditions immediately active, the electrochemical behavior of MgSi was further investigated. This allows estimation of the influence of MgSi precipitates on the corrosion process in the first minutes before Fe-containing intermetallics are active.

As previously mentioned, one unanswered question remains as to what corrosion mechanism causes the pH to increase in MgSi particles and whether MgSi particles can, after initial dissolution, act as cathodic or anodic sites during the corrosion process. In the following sections electrochemical data regarding the evolution of the open circuit potential and the anodic and cathodic behavior are given to clarify these questions.

### 3.2. Corrosion mechanism of MgSi particles at open circuit potential

A combination of open circuit potential measurements and surface analysis can be used to characterize the effect on the corrosion process of exposure-time-related surface modification. It is of course difficult to estimate cathodic or anodic reaction rates with these data alone, but hypotheses on the surface reactivity can be formulated.

In a first step, a detailed AES investigation of the modification experienced by the MgSi particles surface after various immersion conditions was performed. Fig. 8 shows AES depth profiles measured on MgSi. An "as polished" surface was first characterized (Fig. 8a) and a distinct Mg depletion in the surface oxide can be observed. This Mg depletion was obviously provoked by the polishing procedure, even though ethanol was used instead of water. The influence of different surface preparations of Al–Mg–Si alloys on the surface composition is presented elsewhere [36]. Fig. 8b shows the AES depth profile performed on an MgSi particle after immersion in 1 M NaCl with 10 mM $CeCl_3$ for 12 min. The Mg depletion is deeper than the sputtered 0.1 μm and silicon oxide is present on the surface underneath the Ce precipitate.

A further advantage of decorating the particle surface with Ce in solution is that it protects the underlying particles from modification upon subsequent air exposure. It may be concluded that the Si surface is oxidized in solution and that the reactivity of silicon oxide needs to be taken into account. Silicon is also present directly

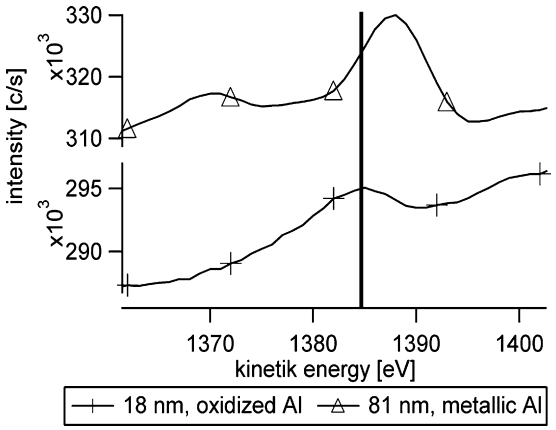


**Fig. 7.** AES spectra of metallic and oxidized Al peak. One curve corresponds to the spectra acquired after 18 nm sputter depth (oxidized). The other curve is from a spectrum after 81 nm sputter depth (metallic).

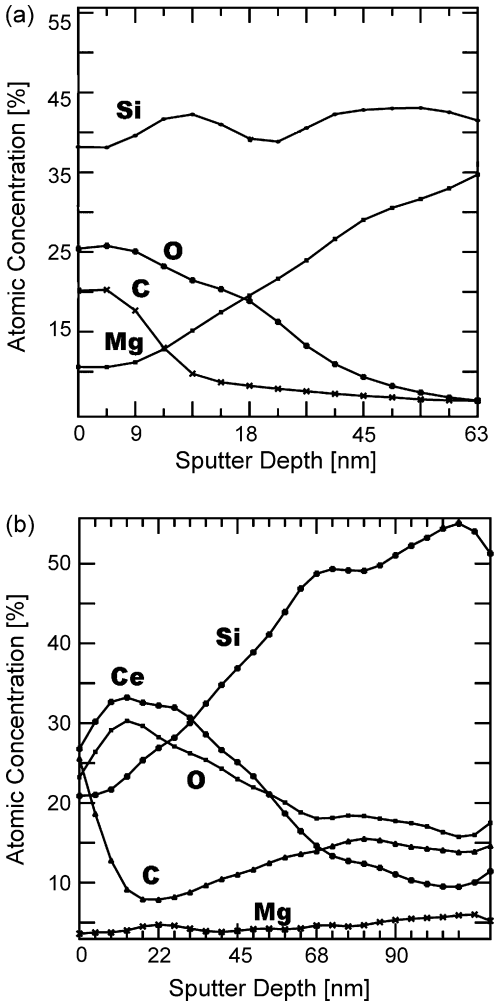


**Fig. 8.** Auger electron spectroscopy depth profile of MgSi particle. (a) Before immersion; (b) after immersion in 1 M NaCl + 10 mM $CeCl_3$ for 12 min.

at the surface, but the exact composition of the layer is difficult to assess because the mixing of the two signals may be the result of a porous Si remnant (as observed by other authors for Cu remnants resulting from the corrosion of Al–Cu–Mg particles [37]).

In addition to "near" surface characterization with AES depth profiles, quantitative EPMA measurements were performed to analyze the in-depth extent of de-alloying. Table 2 presents the Mg/Si wt% ratio and the wt% values for measurements on MgSi and matrix before and after corrosion (30 min in 1 M NaCl). For the matrix it can be seen that Mg does not significantly dissolve, as the ratio with Si changes only slightly. The overall low Mg content in the matrix is caused by the heat treatment.

For MgSi particles a significant depletion of Mg is observable as a result of the corrosion process. The Si content does not change

**Table 2**
Mg and Si content of the AA611 alloys measured quantitatively by EPMA on corroded and uncorroded surfaces

| | Mg/Si ratio | Mg (wt%) | Si (wt%) |
|---|---|---|---|
| MgSi | | | |
| Corroded | 0.5 | 10.22 | 18.30 |
| Uncorroded | 0.9 | 19.50 | 21.50 |
| Matrix | | | |
| Corroded | 0.4 | 0.09 | 0.23 |
| Uncorroded | 0.6 | 0.13 | 0.23 |

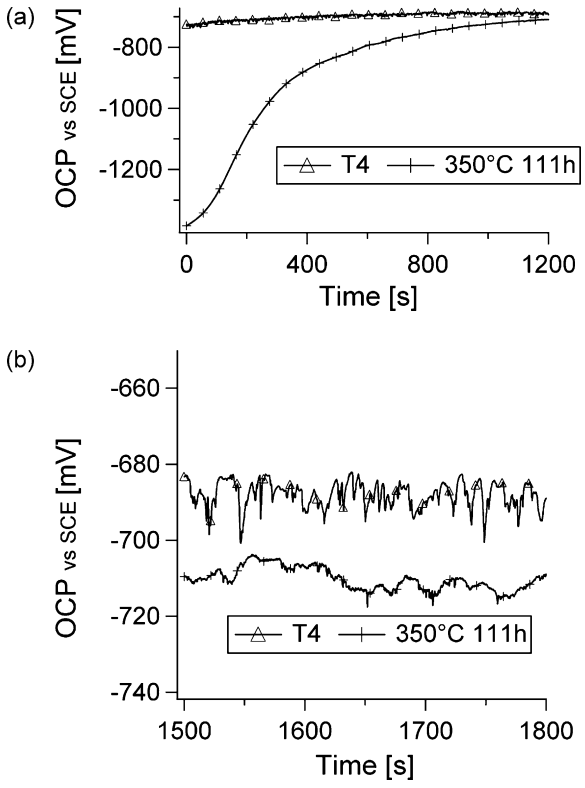


**Fig. 9.** Macroscopic OCP vs. time measurements on a surface in the T4 condition and heat-treated to obtain a high surface fraction of MgSi particles. (a) A starting OCP of −1.5 V is observed, rising to a stable potential of −700 mV. (b) Zoomed area to visualize the OCP difference in the stable potential region.

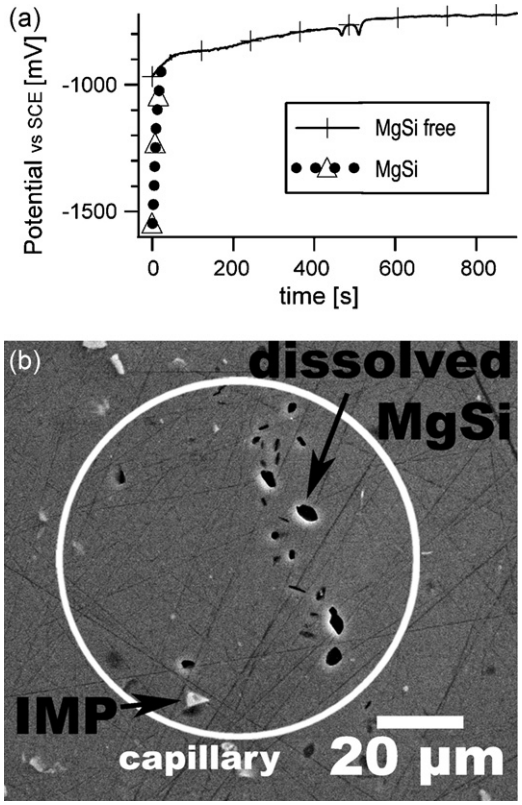


**Fig. 10.** Electrochemical micro-cell measurements with 1 M NaCl. Capillary diameter 80 μm. (a) The OCP evolution as a function of exposure time for a measurement including MgSi and excluding MgSi. (b) SEM image of a surface after stopping the experiment before the OCP reaches a stable level. The MgSi has already been attacked.

much, while almost 50% of the Mg content in MgSi dissolves during corrosion. Thus the change in the Mg/Si ratio is mainly driven by the Mg dissolution.

The Mg/Si ratio for uncorroded MgSi is expected to be 1.72 (Mg/Si ratio for $Mg_2Si$) instead of the value of 1.2 presented in Table 2. This difference is mainly a result of the electron-activated volume (X-rays can travel through more than 3 μm in depth for light metals), which can be larger than the MgSi particles. As the Mg/Si ratio is 0.4 in the matrix and 1.72 in the MgSi particles, the Mg/Si ratio will be modified depending on the volume fraction of matrix in the measured volume. Based on these assumptions, the ratio of 1.2 corresponds to a $Mg_2Si$ particle content of the activated volume of 60 vol%. Further possible reasons for the difference in Mg/Si ratio may be depletion of Mg due to polishing, and the presence of particles with non-stoichiometric composition.

The data presented so far clearly indicate that Mg dissolution takes place during exposure. To monitor this de-alloying process of the surface (already shown ex situ after long exposure times), the open circuit potential (OCP) was recorded as a function of the immersion time of an aged surface (Fig. 9). For comparison, the OCP of a non-heat-treated specimen in the T4 condition was also measured assuming that only minimal MgSi precipitation had taken place in this temper.

The surface, with very little visible MgSi precipitation and a similar amount of Fe-containing intermetallics on the surface (T4 condition), reveals a stable OCP during exposure time compared to the heat-treated specimen (Fig. 9a). The stable OCP is about 20 mV higher than the stable OCP of the heat-treated specimen (Fig. 9b). As after 30 min of immersion, some Mg still remains in the MgSi particles; the slightly lower potential for the heat-treated alloy can be attributed to an ongoing minor dissolution of Mg (Table 2). For the heat-treated specimen, a large surface fraction of MgSi is present (0.6 vol%). Therefore the macroscopic OCP in the beginning seems to be controlled by the Mg dissolution. This assumption is supported by the following arguments: (a) the initial OCP is about −1.38 V vs. SCE (Fig. 9a), which is close to the OCP reported for synthesized $Mg_2Si$ by Buchheit [26,38]; (b) activation due to trace elements is not possible as the specimen is polished after heat treatment [39]; (c) a similar effect was measured by Wloka and Virtanen [30] in a different alloy.

To prove that the low starting OCP is induced by active Mg dissolution, additional electrochemical micro-cell (eMC) experiments were performed. The main advantage of the local micro-cell experiments is an exact correlation between electrochemical information (in this case OCP) and microstructural features. Fig. 10a shows the evolution of the OCP of an eMC measurement, including a large amount of MgSi and also matrix and Fe-intermetallics. The micro-cell experiment on an area including MgSi was stopped after 22 s to analyze the surface change before stable OCP is reached. It can be seen that the MgSi particles have already been attacked (Fig. 10b) and that therefore the rise in OCP can be attributed to the Mg dissolution. The attack on MgSi within seconds was also reported by Yasakau et al. [25] in AA5xxx alloys. However, the rise in the OCP is very fast compared to the macroscopic OCP measurements. There are two reasons for this: (a) due to the shape of the capillaries hemispherical diffusion can take place. Higher dissolution rates of Mg are therefore to be expected; (b) the OCP in an electrochemical micro-cell experiment is influenced by single inclusions and therefore no statistical distribution of the initiation time of the dissolution process can be expected in single measurements.

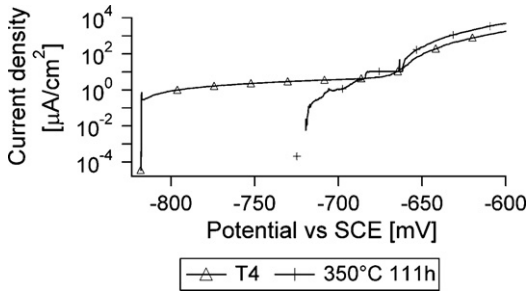


**Fig. 11.** Comparison of macroscopic anodic potentiodynamic polarization measurements on a surface for two alloy microstructures: (i) in the T4 condition and (ii) heat-treated at 350 °C for 111 h to obtain a high surface fraction of MgSi particles. No preferential pitting susceptibility for the MgSi.

It can additionally be seen that the OCP of an area which includes only Fe intermetallics (called "MgSi free"; still measured on the same specimen as the measurement on the MgSi-containing area) behaves similarly to the macroscopic measurements in the T4 condition. This series of experiments proves that the presence of MgSi is the cause of the low initial OCP, and that Mg dissolution triggers the fast rise of the OCP at the beginning of exposure. Areas excluding MgSi particles seem to behave similarly in terms of OCP evolution for both conditions (T4 and heat-treated).

In summary, it was found for the open circuit behavior of MgSi particles that Mg starts to dissolve immediately, reaching a stable situation after 20 min when macroscopic OCP characterizations are performed. The open circuit potential at the beginning of immersion is controlled by the active dissolution of Mg. Cathodic polarization of Al during the first few minutes is therefore to be expected. At the time where the open circuit potential reaches a stable plateau, Fe-containing intermetallics become cathodically active. However, even after characterization of the Mg dissolution process and the MgSi remnant, the role of this remnant in the localized corrosion process is still unclear. In the further investigation step, potentiodynamic polarization experiments were performed, in order to estimate the role of MgSi remnants as anodic and cathodic sites.

### 3.3. Influence of MgSi particle remnants on anodic behavior

In the case of Al alloys, measuring the anodic electrochemical behavior of a surface reveals initiation sites and resistance against localized corrosion. In this section, MgSi precipitates are analyzed with respect to their susceptibility and importance as localized corrosion initiation sites after de-alloying. In this context, there is often confusion in the literature between pure de-alloying processes which occur in intermetallic particles and in depth localized corrosion propagation. Those two processes are often unrelated.

Fig. 11 presents the anodic potentiodynamic polarization curves for an alloy in T4 condition (small number of MgSi precipitates), heat-treated at 350 °C for 111 h to obtain a large surface fraction of MgSi precipitates. Before polarization, the surfaces were immersed in 1 M NaCl solution for 30 min. During this immersion time, MgSi particles are de-alloyed and Si remnants are present on the surface.

The pitting potential (potential where a strong current increase is recorded after passive behavior) is for both heat treatments (with and without a large number of MgSi particles) in the same range of −665 mV vs. SCE. Therefore MgSi particles are not seen as preferential sites for localized corrosion initiation after de-alloying. This accords with previous work [30,31] but contradicts the findings of Mankowski, where a preferential initiation for deep attack at MgSi was reported from interferometry and surface examination [7,40].

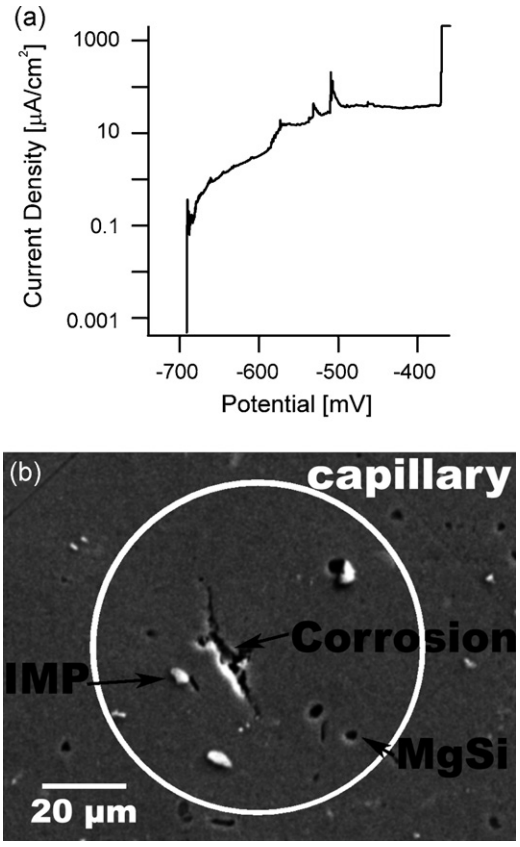


**Fig. 12.** Electrochemical micro-cell measurement on a surface containing MgSi. (a) Current density vs. applied potential (vs. SCE). (b) Corresponding surface after the polarization experiment. The onset of localized corrosion cannot be attributed to MgSi.

To observe single selected initiation sites, electrochemical micro-cell measurements were also performed. The advantage of using this local electrochemical method is as already mentioned, that single corrosion events can be correlated with microstructural features and selected areas can be measured. Fig. 12 shows the potentiodynamic polarization curve and the corresponding SEM image of the surface. Before the polarization experiment the surface was held for 30 min at OCP.

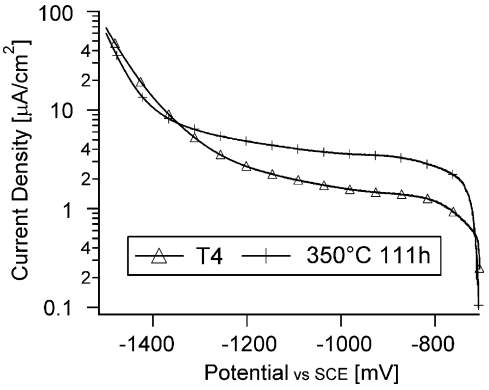


**Fig. 13.** Macroscopic cathodic potentiodynamic polarization measurement of a surface in the T4 condition and heat-treated at 350 °C for 111 h to obtain a high surface fraction of MgSi particles. The surfaces were exposed to 1 M NaCl for 30 min before polarization. The surface of the T4 condition shows a lower cathodic current density than that with a high MgSi density.

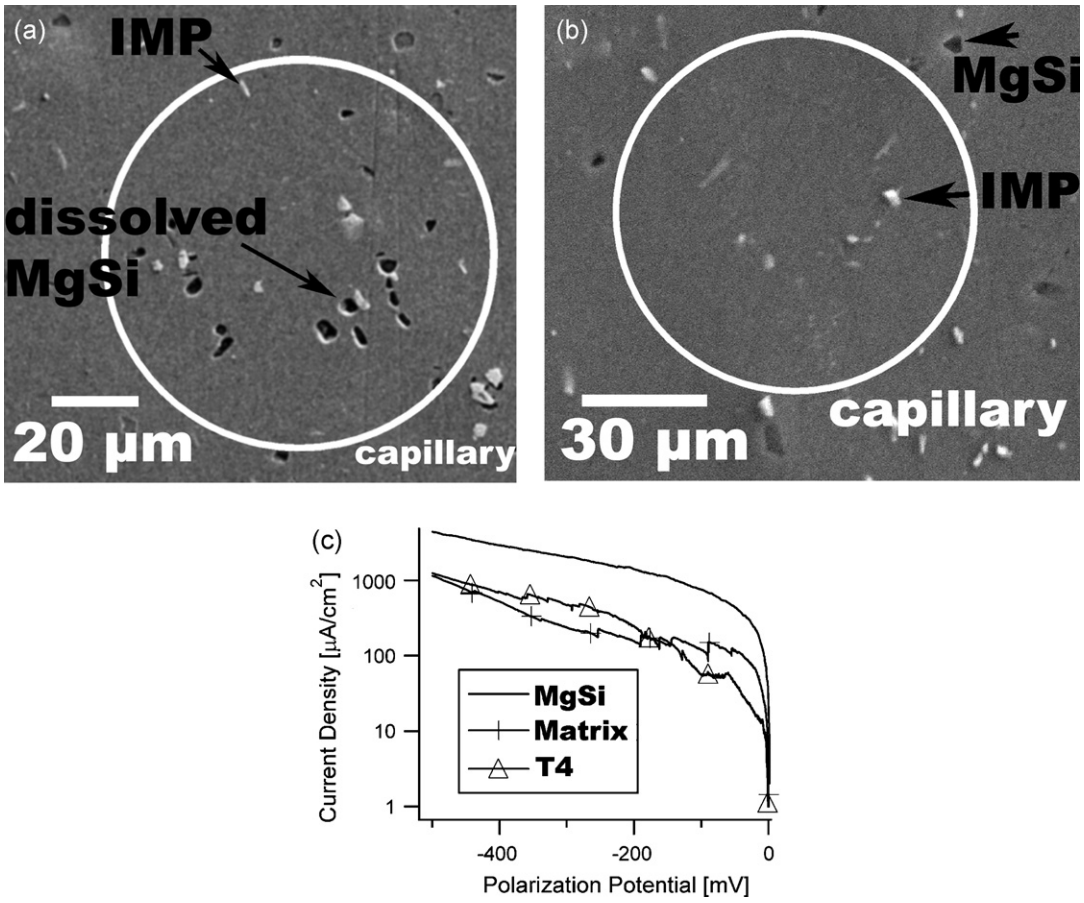


**Fig. 14.** Electrochemical micro-cell measurements on an area including: (a) MgSi; (b) only matrix; (c) comparison of the cathodic potentiodynamic polarization curves of the areas seen in (a) and (b) plus an area on a specimen in T4 temper (small amount of MgSi). The potentials are given relative to the OCP for better comparison.

In the micro-cell measurement, the pitting potential is higher than in the macroscopic measurement. This frequently observed increase is related to the fact that a smaller measurement area includes less highly susceptible initiation site [21,41]. The corrosion started in the middle of the area exposed by the capillary (IGC type) and the previously de-alloyed MgSi particles show no evidence of acting as further corrosion propagation sites (Fig. 12b).

From these measurements it is clear that the microscopic MgSi remnants are not preferred anodic initiation sites and therefore have only a minor influence on the corrosion propagation phenomena. The absence of corrosion propagation at the MgSi remnants is also supported by the fact that a high local pH is measured, which in some way hinders stable pit growth conditions.

Whether this pH raise is only due to Mg dissolution and therefore stops after about 20 min (as described in Fig. 10) or whether it continues depends on the cathodic activity of the MgSi remnant. In the following section cathodic potentiodynamic polarization curves are therefore measured to characterize the cathodic reactivity of MgSi remnants.

### 3.4. Influence of MgSi particle remnants on cathodic activity

In this section, the influence of de-alloyed MgSi precipitates on cathodic electrochemical activity is discussed. This issue is especially interesting, as Fe-containing intermetallics do not contribute to the oxygen reduction rate at the outset of the corrosion process when the surface is aged in air. The cathodic activity of MgSi remnants is also of interest because of the high local pH observed above MgSi particles.

Fig. 13 provides the cathodic potentiodynamic polarization curves of the alloy in the T4 condition and heat-treated at 350 °C for 111 h. The surfaces were immersed in 1 M NaCl for 30 min before the polarization began. It can be observed that the surface with the high MgSi surface fraction has a current density about three times higher than the surface in T4 condition.

At −1.0 V vs. SCE (middle of oxygen reduction plateau), for example, the surface in the T4 condition exhibit a current density of 2 μA/cm$^2$, while heat-treated specimen shows a current density of 6 μA/cm$^2$. If the difference of 4 μA/cm$^2$ is attributed completely to the MgSi remnant, the effective current density induced by this remnant can be calculated. The MgSi density in the alloy must be measured, first via tomograms like the one shown in Fig. 1. With these data, a volume and surface area fraction of 0.6 ± 0.08% was obtained for the heat-treated specimen. Taking this surface reacting area into account, a current density of about 0.6 mA/cm$^2$ (at a potential of −1.0 V vs. SCE) has to be generated by the MgSi remnant. Baek and Frankel [42] found cathodic current densities of about 0.1 mA/cm$^2$ on AA2024 in the cathodic plateau region and for pure Al a current density about one order of magnitude lower. This generates a current density of 10–100 mA/cm$^2$ sustained by the particles, assuming a particle density of 1–10%. For binary Al–Fe model alloys Ambat et al. [5] found cathodic current densities of 0.1 mA/cm$^2$ in pH 3 solutions, which gives a Fe intermetallic current density of about 10 mA/cm$^2$. The particle density is about 1% and it is assumed that only the intermetallics are responsible for the cathodic current change between pure Al and Al with 0.42% Fe. Chen and Kucernak [43] reported oxygen reduction rates on Pt of 10 mA/cm$^2$ (12 μm dots) to 50 mA/cm$^2$ (4 μm dots). This shows that the measured oxy-

gen reduction rate of 0.6 mA/cm$^2$ for the MgSi remnants is lower than the values for active elements like Cu or catalytic Pt, but in a measurable range.

To directly prove the influence of MgSi remnants on the cathodic current, additional electrochemical micro-cell measurements were performed. The results are shown in Fig. 14. Potentiodynamic cathodic polarization was started again after exposing the surface to 1 M NaCl for 30 min. Fig. 14a shows the measured surface, including MgSi, after the cathodic polarization experiment. The dissolution of MgSi is clearly visible. In Fig. 14b, the area excluding MgSi is shown; no corrosion resulting from the OCP conditioning or the following cathodic polarization is visible.

Fig. 14c shows the cathodic polarization curves measured on an area including MgSi, including only Fe-containing IMP (both on the same specimen heat-treated at 350 °C for 15 h) and measured on a specimen in the T4 temper. The potential is set to zero for the OCP (overpotential representation) to better compare the cathodic current densities resulting from the various surface conditions. The cathodic current densities of areas excluding MgSi (heat treatment 350 °C, 15 h) and on a random chosen surface in the T4 temper are similar. On both surfaces, a similar number of Fe-containing intermetallics and small quantities of small precipitates are present. In micro-cell measurements the current density difference between an area including no MgSi and including MgSi is about 1000 μA/cm$^2$ (a factor of about 10). A current density of about 40 mA/cm$^2$ evolving at MgSi remnants can be calculated considering the higher MgSi surface fraction of 2.6% in the micro-capillary. This cathodic current density is $10^2$ times higher than the value measured with a macroscopic cell (macroscopic 0.5 mA/cm$^2$, microscopic 40 mA/cm$^2$). This difference can be caused by the difference in the diffusion rates and type. Due to the form of the capillary a fast diffusion (towards hemispherical diffusion rates) can be assumed, allowing higher oxygen reduction rates. A rise of cathodic currents of $10^2$ with an area decrease of $10^3$ on stainless steel was also reported by Birbilis et al. [44] and support the findings made in this study (where the area of the micro-cell is $10^4$ smaller than that of the macro-cell).

These electrochemical polarization experiments indicate that very high cathodic current densities can be achieved on local cathodes and that the MgSi remnants are cathodically active. This cathodic activity is roughly 1–2 orders of magnitude below that reported for Cu-containing intermetallics, but is still significant.

## 4. Conclusions

In this study, the behavior of MgSi particles during Al–Mg–Si alloy corrosion processes was characterized. Ce decoration experiments, open circuit measurements, cathodic and anodic potentiodynamic polarization in both macroscopic and electrochemical micro-cell experiments were used to obtain detailed information on the microscopic location and kinetics of the electrochemical reactions. The surface was characterized ex situ using AES and EPMA techniques, to investigate the local modification of the material surface resulting from the corrosion processes.

The influence of MgSi particles on the corrosion process can be described as follows:

(a) Mg dissolution on MgSi particles starts already after just a few seconds of immersion regardless of the aging condition. The measured open circuit potential of the alloy is controlled by the active Mg dissolution, when a surface fraction of about 0.6% MgSi particles is present. A local increase in the pH above dissolving MgSi particle can be detected.

(b) A Si-rich remnant with an oxidized surface is left after the de-alloying process has taken place.

(c) MgSi does not serve as an anodic a corrosion propagation site after de-alloying. This conclusion is also supported by the observed pH rise in dissolving MgSi particles.

(d) MgSi remnants are cathodically active and raise the measured cathodic current by a factor of 3 compared to MgSi excluding surfaces. In microscopic experiments the difference is a factor of 10, as the surface fraction of MgSi may rise in the measuring area and faster diffusion can take place in the used capillary. With a cathodic current density about 10 times smaller than that reported for Cu, MgSi remnants can still cathodically promote corrosion if, e.g., other intermetallics are inactive. This is the case, i.e., for short exposure times where the large Fe-containing intermetallics can be inactive.

## Acknowledgements

The authors gratefully acknowledge funding by the Alcan Technology Fund from the ETH domain. The authors would like to thank R. Hauert for his support with the Auger measurements.

## References

[1] W.S. Miller, L. Zhuang, J. Bottema, A. Wittebrood, P. De Smet, A. Haszler, A. Vieregge, Mater. Sci. Eng. A: Struct. Mater. Prop. Microstruct. Process. 280 (2000) 37.
[2] D.G. Altenpohl, Aluminum: Technology, Applications, Environment, The Aluminum Association, 1998.
[3] J. Zahavi, J. Yahalom, J. Electrochem. Soc. 129 (1982) 1181.
[4] G. Svenningsen, J.E. Lein, A. Bjorgum, J.H. Nordlien, Y.D. Yu, K. Nisancioglu, Corros. Sci. 48 (2006) 226.
[5] R. Ambat, A.J. Davenport, G.M. Scamans, A. Afseth, Corros. Sci. 48 (2006) 3455.
[6] J.M.C. Mol, B.R.W. Hinton, D.H. van der Weijde, J.H.W. de Wit, S. van der Zwaag, J. Mater. Sci. 35 (2000) 1629.
[7] V. Guillaumin, G. Mankowski, Corros. Sci. 42 (2000) 105.
[8] C.-M. Liao, R.P. Wei, Electrochim. Acta 45 (1999) 881.
[9] C. Blanc, G. Mankowski, Corros. Sci. 40 (1998) 411.
[10] K. Nisancioglu, J. Electrochem. Soc. 137 (1990) 69.
[11] F. Andreatta, M.M. Lohrengel, H. Terryn, J.H.W. de Wit, Electrochim. Acta 48 (2003) 3239.
[12] O. Lunder, K. Nisancioglu, Corrosion 44 (1988) 414.
[13] A.J. Aldykiewicz, H.S. Isaacs, A.J. Davenport, J. Electrochem. Soc. 142 (1995) 3342.
[14] R.G. Buchheit, S.B. Mamidipally, P. Schmutz, H. Guan, Corrosion 58 (2002).
[15] A.J. Davenport, H.S. Isaacs, M.W. Kendig, Corros. Sci. 32 (1991) 653.
[16] B.R.W. Hinton, D.R. Arnott, N.E. Ryan, Met. Forum 7 (1984) 211.
[17] M. Pourbaix, NACE Cebelcor 290 (1974).
[18] M. Kendig, S. Jeanjaquet, R. Addison, J. Waldrop, Surf. Coat. Technol. 140 (2001) 58.
[19] C. Blanc, G. Mankowski, Corros. Sci. 39 (1997) 949.
[20] T. Suter, R.C. Alkire, J. Electrochem. Soc. 148 (2001) B36.
[21] J.E. Hatch, Am. Soc. Met. (1984).
[22] L.F. Mondolfo, Aluminum Alloys, Structure and Properties, 1976.
[23] O. Lunder, J.C. Walmsley, P. Mack, K. Nisancioglu, Corros. Sci. 47 (2005) 1604.
[24] K. Mizuno, A. Nylund, I. Olefjord, Corros. Sci. 43 (2001) 381.
[25] K.A. Yasakau, M.L. Zheludkevich, S.V. Lamaka, M.G.S. Ferreira, Electrochim. Acta 52 (2007) 7651.
[26] R.G. Buchheit, J. Electrochem. Soc. 142 (1995).
[27] S.M. Hirth, G.J. Marshall, S.A. Court, D.J. Lloyd, Mater. Sci. Eng. A: Struct. Mater. Prop. Microst. Process. 319 (2001) 452.
[28] I.R. Harris, P.C. Varley, J. Inst. Met. 82 (1954) 379.
[29] J.M.C. Mol, J.V. de Langkruis, J.H.W. de Wit, S. van der Zwaag, Corros. Sci. 47 (2005) 2711.
[30] J. Wloka, S. Virtanen, J. Electrochem. Soc. 154 (2007) C411.
[31] F. Eckermann, T. Suter, A. Afseth, P.J. Uggowitzer, M. Stampanoni, F. Marone, P. Schmutz P. J. Electrochem. Soc., in press.
[32] G.M. Scamans, A. Afseth, G.E. Thompson, Y. Liu, X. Zhou, Aluminium Alloys 519–521 (Pts 1 and 2) (2006) 647.
[33] C.L. Hedberg (Ed.), Handbook of Auger Electron Spectroscopy, Physical Electronic Inc., Eden Prairie, MN, 1995.
[34] T. Suter, H. Boehni, Electrochim. Acta 42 (1997) 3175.
[35] G.L. Song, A. Atrens, Adv. Eng. Mater. 1 (1999) 11.
[36] B.S. Tanem, G. Svenningsen, J. Mardalen, Corros. Sci. 47 (2005) 1506.

[37] R.G. Buchheit, R.P. Grant, P.F. Hlava, B. McKenzie, G.L. Zender, J. Electrochem. Soc. 144 (1997) 2621.
[38] N. Birbilis, R.G. Buchheit, J. Electrochem. Soc. 152 (2005) B140.
[39] J.T.B. Gundersen, A. Aytac, S. Ono, J.H. Nordlien, K. Nisancioglu, Corros. Sci. 46 (2004) 265.
[40] C. Blanc, Y. Roques, G. Mankowski, Corros. Sci. 40 (1998) 1019.
[41] T. Suter, Y. Muller, P. Schmutz, O. von Trzebiatowski, Adv. Eng. Mater. 7 (2005) 339.
[42] Y. Baek, G.S. Frankel, J. Electrochem. Soc. 150 (2003) B1.
[43] S.L. Chen, A. Kucernak, J. Phys. Chem. B 108 (2004) 3262.
[44] N. Birbilis, B.N. Padgett, R.G. Buchheit, Electrochim. Acta 50 (2005) 3536.